Focus Section: Deformation Models of Fault Slip for the 2023 Update

NeoKinema Deformation Model for the 2023 Update to the U.S. National Seismic Hazard Model

Zheng-Kang Shen[*1] and Peter Bird[1]

Abstract

We develop a crustal deformation model of the western conterminous United States for the 2023 update of the National Seismic Hazard Model (NSHM). The kinematic finite-element code NeoKinema is used to describe crustal deformation, including long-term slip on faults and off-fault strains (both elastic and permanent). Three different data sets—Global Positioning System (GPS) velocities, geological fault offset rates, and crustal stress orientations—are used to constrain the model, and the plate tectonic rotation of Pacific relative to North America is also imposed on some boundaries. Compared to the last NSHM model update in 2014, the GPS and geological fault data are substantially updated, and new corrections are implemented in both the data and modeling approach, including the correction of the "ghost transient" effect due to postseismic deformation following large historic earthquakes, and correction for shallow creep on faults estimated from independent data. Based on these modeling results and a plate tectonic model of the Cascadia subduction zone, a long-term seismicity rate map is also computed for the western United States; this map is independent of the local seismic catalog and can, therefore, be tested retrospectively as well as prospectively. We find good success in most of the region, except in Cascadia, where the 45 yr instrumental seismicity record is much quieter than the forecast of our long-term model.

Cite this article as Shen, Z.-K., and P. Bird (2022). NeoKinema Deformation Model for the 2023 Update to the U.S. National Seismic Hazard Model, *Seismol. Res. Lett.* **XX**, 1–16, doi: 10.1785/0220220179.

Supplemental Material

Introduction

The west coast of the continental United States lies along tectonic plate boundaries, where the Pacific plate moves northwestward relative to the North America plate across the San Andreas fault system in California, and the Juan de Fuca plate plunges underneath the Pacific Northwest region along the Cascadia subduction zone. Across the plate-boundary zone deformation is widespread, extending hundreds of kilometers into the interior of the North America plate and causing distributed faulting and earthquakes. To mitigate the earthquake hazard, the U.S. Geological Survey (USGS) has developed the National Seismic Hazard Model (NSHM) over the past half century to provide probabilistic hazard information about the seismogenic faults, their long-term slip rates, and associated ground-shaking potentials. The next NSHM is scheduled for release in 2023, and this study is to contribute to this endeavor by providing an update of the solution for fault-slip rates and off-fault deformation rates, constrained by geological and geodetic observations, using the kinematic finite-element code NeoKinema.

The finite-element modeling approach used by NeoKinema is to integrate geological fault offset rates, geodetic velocities, and crustal stress orientations and solve long-term fault offset rates and off-fault strain rates (Liu and Bird, 2008; Bird, 2009). During the last update of the NSHM (NSHM2014), NeoKinema contributed to the solution for the western United States (Powers and Field, 2015). NeoKinema also contributed to the last update of the model for the Uniform California Earthquake Rupture Forecast (Version 3) (UCERF3; Field *et al.*, 2013). For this new update of the NSHM for the western United States, the input data have been much improved. The number of mapped active and potentially active faults is increased from 668 to 1017, and all these new faults also have associated geologic estimates of their long-term slip rates (with broad uncertainties). The Global Positioning System (GPS) sites are densified, particularly in the Basin and Range, Yellowstone, and Wasatch fault areas, and longer observation histories for some sites permit better velocity estimates and accuracy (Zeng, 2022). This round of the NSHM deformation modeling also takes into account two corrections to the GPS data input. One correction is for the

1. Department of Earth, Planetary, and Space Sciences, UCLA, Los Angeles, California, U.S.A., https://orcid.org/0000-0002-4965-174X (Z-KS); https://orcid.org/0000-0001-9034-1287 (PB)

*Corresponding author: zshen@ucla.edu

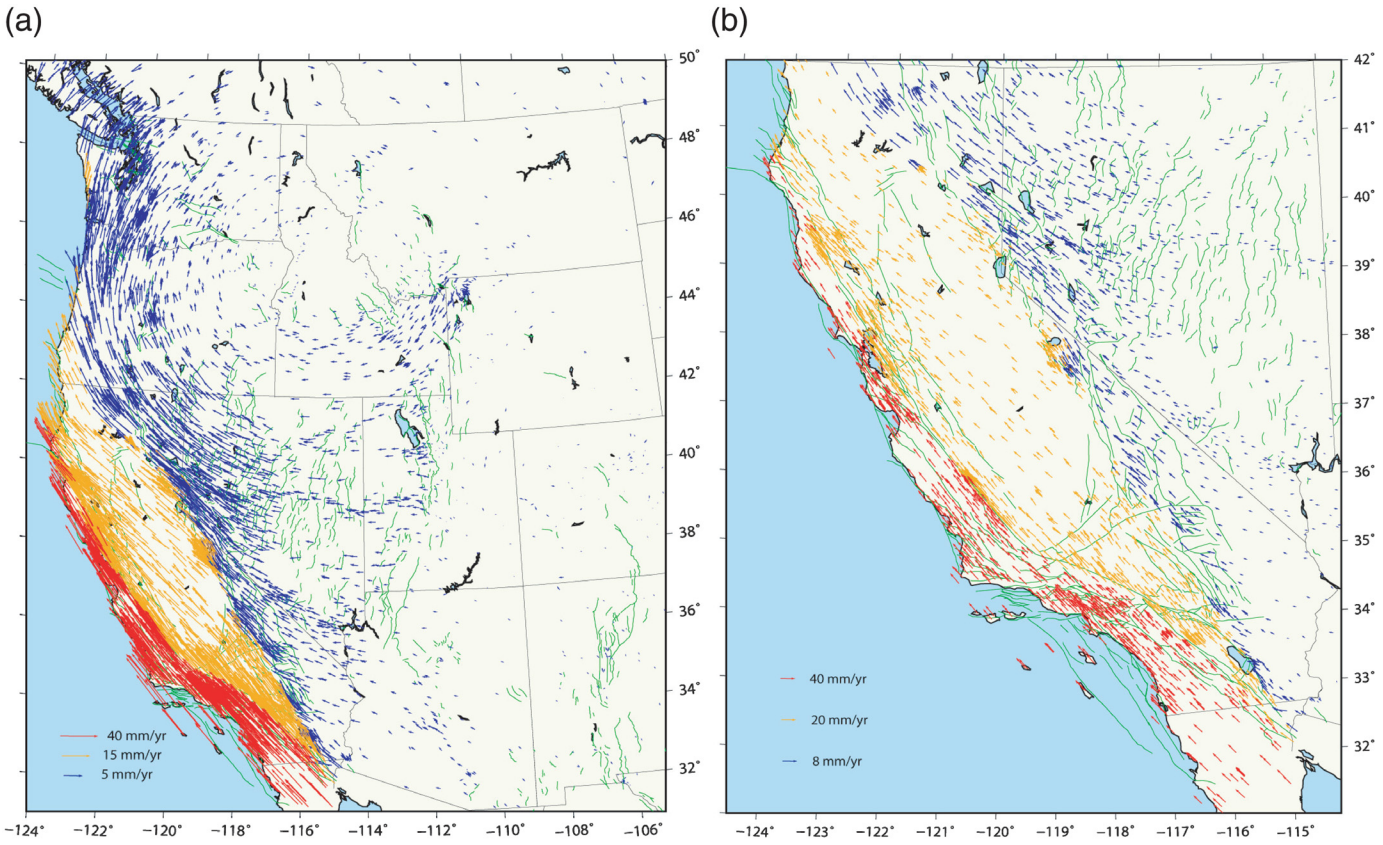

Figure 1. Western U.S. Global Positioning System (GPS) velocity data referenced to stable North American plate. Data are plotted with three color scales: 0–10 mm/yr, blue; 10–30 mm/yr, orange; and 30–50 mm/yr, red. Green lines are surface traces of active and potentially active faults included in this study. (a) Western U.S. region. (b) Southwest U.S. region.

transient deformation caused by postseismic deformation of large historic earthquakes, to meet the model assumption that GPS data reflect quasi-time-independent interseismic deformation. This transient correction is referenced to deformation averaged over many earthquake cycles and converts the strain rate pattern observed today to the hypothetical strain rate pattern observed over an average interseismic period (Hearn *et al.*, 2013; Devries *et al.*, 2017; Pollitz and Evans, 2017). The other correction is for effects of shallow creep on faults, such that the fault-locking effect can be uniformly modeled for the ultimate estimation of the long-term fault offset rates. In the final result, we present a long-term crustal deformation model including both fault slip and off-fault permanent deformation and an associated seismicity model for the western United States.

GPS Velocity Data

GPS data have been collected over the western United States in the past three decades, and the data were processed by various groups to derive secular station velocities relative to stable eastern North America. A composite velocity data set of 4978 sites has been produced (Zeng, 2022) by combining multiple solutions from campaign and continuous networks.

We have filtered this data set by (1) decimating the collocated sites (<1 km separation), (2) removing obvious outliers shown in model postfit residuals (such as displacements due to geothermal activity and/or singularities at sites away from active faults), and (3) removing sites located in "fault corridors" of finite elements (~2 km width) along faults with slip rates of >1 mm/yr, because these velocities would not be modeled properly by our algorithm. Velocities of 4312 sites are retained after data cleaning (Fig. 1; Table S1, available in the supplemental material to this article).

Only the horizontal components of these GPS velocity vectors are used in this project. In general, our assumption is that these horizontal velocities reflect interseismic time windows, in which the GPS velocity field is laterally continuous. During the NeoKinema modeling process, these interseismic velocities are converted to estimates of long-term-average velocities by addition of mean rates of coseismic displacements; this correction is iterated as model estimates of fault-slip rates change during the iteration of any solution.

There are also four corrections and changes performed for the GPS velocity data.

1. Correction for ghost transient deformation due to past earthquakes. Large earthquakes induce transient visco-elastic deformation of the lower crust and upper mantle, which

can last for decades or even centuries. Temporal variations in postseismic relaxation results in the geodetic deformation rate at a given time deviating from the ideal long-term interseismic deformation rates averaged over many thousands of years. To construct the best possible time-independent seismic hazard model, such ghost transient effects should be removed from the data used to constrain the model. Hearn (2022) has developed a visco-elastic model and forward-predicted ghost transient velocities caused by past large earthquakes (e.g., 1857 and 1906 earthquakes on the San Andreas fault). Such ghost transient is referenced to the earthquake cycle averaged deformation, and we have used the ghost transient velocities to correct the GPS velocity data to be used in our model.

2. Correction for fault creep effect. Most of the western U.S. faults are locked in the upper crust layer interseismically, except for a few such as the central California creeping section of the San Andreas fault and the Hayward fault, which are creeping or partially creeping in the upper crust section interseismically. The crustal deformation models often assume that interseismic fault slip is only below the locking depth, which defines the base of seismic ruptures; if so, corrections are required for GPS data collected near to faults with shallow creep. Johnson *et al.* (2022) produced such corrections for GPS velocity data using Interferometric Synthetic Aperture Radar and short baseline data measured across the creeping or partially creeping faults in California, including the Calaveras, Hayward, Maacama, and Barlett Springs faults in northern, the creeping section of the San Andreas in central, and the Imperial fault in southern California. They interpreted interseismic velocities of the geodetic data by a model with block motion between faults and backslip on fault due to fault locking and used the model to predict surface displacements due to fault creep or partial creep within the seismogenic depth. These model-predicted near-fault velocities are used to correct the GPS data set that is used in this study.
3. Correction for Cascadia megathrust fault locking effect. The interseismically locked section of the Cascadia megathrust is located offshore of the Pacific Northwest and is not included as a deformation source for some crustal deformation modeling studies. The elastic deformation due to megathrust fault locking, however, has imprints across the surface of the continent, and the effect needs to be corrected for the GPS data to be used in deformation models not including the megathrust as a deformation source. We incorporate such corrections for a GPS velocity data set derived from a deformation model for the Pacific Northwest region (McCaffrey *et al.*, 2013). We correct our data set using corrections for the GPS sites existing in both of McCaffrey *et al.*'s and our data sets. For the new sites in our current data set, we search for nearby sites in the old data set as surrogates for correction, as differences for the correction terms between nearby sites in the densely populated data set are very small, and their omission has almost no effect on the solution.
4. Redefinition and increased estimates of uncertainties in GPS velocity data. The GPS velocity data set is composed from multiple data sources, including both campaign and continuous GPS observations. The uncertainties were derived in various ways, and are not intrinsically consistent. Certain epistemic errors are not accounted for in their uncertainty evaluation, such as local monument instability, antenna setup error, nontectonic motion such as that due to hydraulic circulation, error due to reference inconsistency between different data sets, and so forth. Current uncertainties for some continuous GPS sites, for example, are nominally as small as ∼0.1 mm/yr, which are unlikely to reflect the true uncertainty of thousand-year bedrock interseismic motion at the site (Bird and Carafa, 2016). To model such epistemic, shallow-deformation, and/or transient-deformation errors, we impose an ad hoc minimum uncertainty $\sigma_m = 0.3$ mm/yr and replace all the uncertainties σ_i for the GPS horizontal components with

$$\sigma_i \leftarrow (\sigma_{m^2} + \sigma_{i^2})^{1/2}.$$

This ad hoc minimum uncertainty is chosen based on our past experience (e.g., Shen *et al.*, 2011).

Geological Fault and Slip Model

Generations of geological fault-trace and fault-slip models have been used in the production of seismic hazard models for the western United States, and the last version of the model was used for the 2014 NSHM. The model we are using this time is an update of the 2014 model by Hatem et al. (Hatem, Collett, *et al.*, 2022; Hatem, Reitman, *et al.*, 2022), with more than 300 minor (i.e., short and/or slow-moving) faults added. The total number of faults is 1017. In the model each fault is defined with fault-trace location coordinates, dip angle, rake angle, and upper and lower locking depths. Minimum and maximum slip rates are assigned for all the faults, but preferred fault-slip rates are provided for only some of the faults.

One difference of the 2022 model (Hatem, Reitman, *et al.*, 2022) from the NSHM2014 model is that in the 2022 model, the San Andreas fault system was not extended down to the Gulf of California and Sea of Cortes, but ended at the southern end of the Imperial fault at ∼32.3° N. Such a model would not match the GPS data from the international border region and from northern Mexico. We search the 2014 NSHM fault database and add three other fault segments: the "NA–PA transform 1 in northern Gulf of California," the "NA–PA ridge 1 in northern Gulf of California," and the "NA–PA transform 2 in northern Gulf of California" segments, which extend the fault system southeastward to latitude 30.3° N. The surface traces of the fault model are shown in Figure 2, and the digitized fault traces are documented in Table S2.

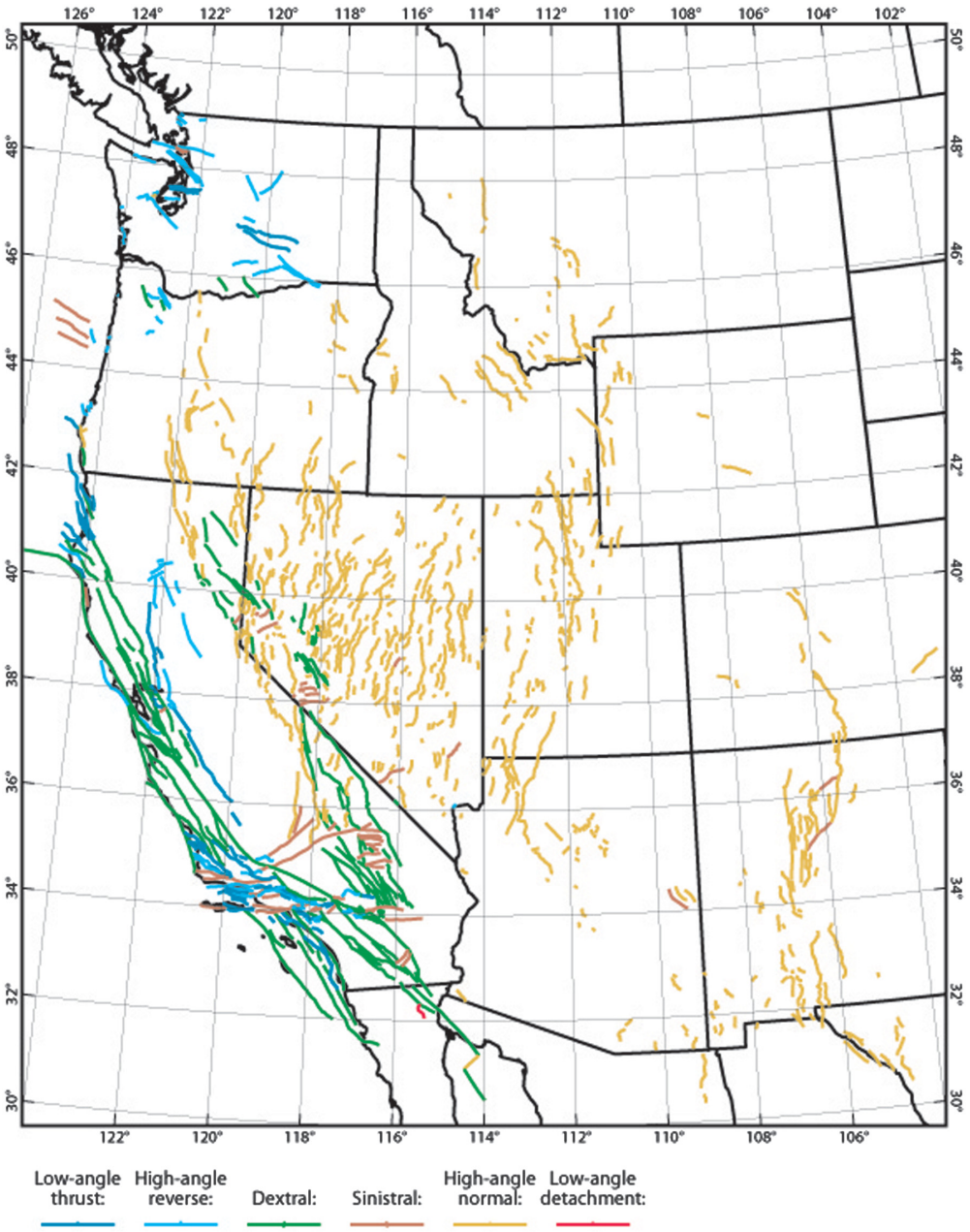

Figure 2. Geological faults whose neotectonic deformation is modeled in this study.

We convert fault-slip rate data from the geologic model into geological constraints for NeoKinema modeling. For each fault segment, the target fault-slip rate is taken as the geologic "preferred" slip rate, or if a preferred rate is not available, the average value of the minimum and maximum slip rates is adopted instead. The half width of the difference between the minimum and maximum rates is taken as the standard error. The lower and upper bounds of the slip rate in our NeoKinema models are set at 0.75 times the geological minimum rate and 1.25 times the geological maximum rate, respectively. A retrospective justification for this choice is included in the Discussion section.

Some of the faults are defined as pure strike slip or thrust and normal slip. If the fault-slip rate is significant (several millimeters per year or larger), we allow a nonvertical fault to slip with an orthogonal rake as well but constrain that component of slip to a moderate rate. We also change the dip angle of the modeled Brawley fault from 90° to 45° to allow a normal component of motion across the fault (and/or dike injection along the fault). This change improves local data fitting significantly.

NeoKinema Crustal Deformation Modeling of Western United States

NeoKinema is a kinematic finite-element code to model neotectonic crustal deformation caused by fault slip, constrained by geological fault-slip rates, tectonic stress orientations, and GPS velocities. The optimal solution is obtained by minimizing an objective function, which is a function of model predictions ($\underline{p}$) and corresponding data values ($\underline{r}$), normalized by covariance matrix (C, for GPS velocities only) or by datum standard deviations ($\underline{\sigma}$):

$$\prod = (\underline{p}-\underline{r})^T C_{\text{gps}}^{-1}(\underline{p}-\underline{r}) - \frac{1}{L_0}\sum_{m=1}^{M}\int_{\text{length}(m)}\frac{(p_m-r_m)^2}{\sigma_m^2}dl - \frac{1}{A_0}\sum_{n=1}^{N}\iint_{\text{area}}\frac{(p_n-r_n)^2}{\sigma_n^2}da. \quad (1)$$

In the first term, $\underline{p}$ and $\underline{r}$ are model predicted and observed horizontal GPS velocity components, and C_{gps} is the covariance matrix of horizontal GPS velocity components. In the second term, $\underline{p_m}$ and $\underline{r_m}$ are model predicted and geologically observed fault offset rates, and $\underline{\sigma_m}$ are their standard errors. In the third term, $\underline{p_n}$ and $\underline{r_n}$ are model predicted and observed

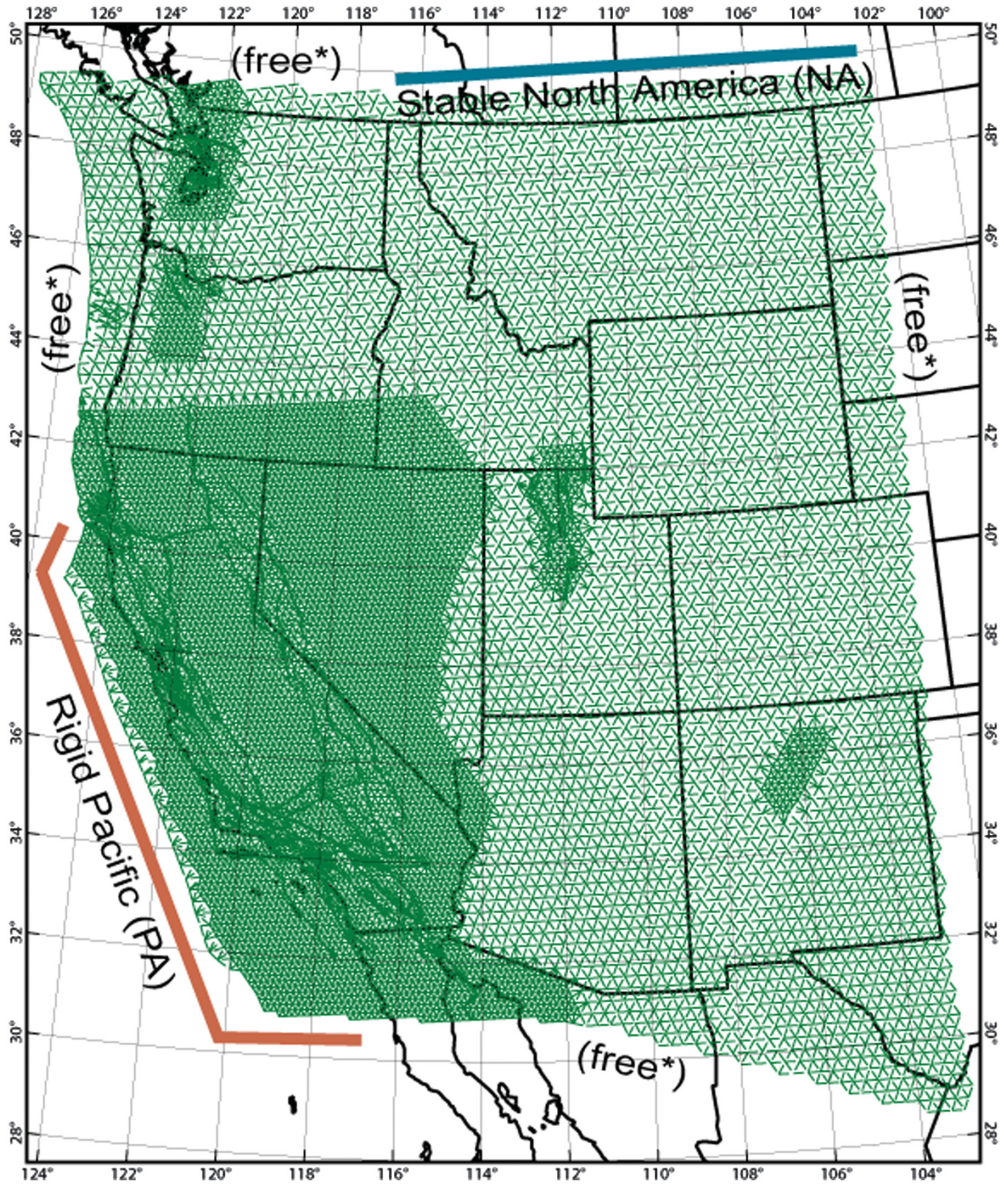

Figure 3. Finite-element grid for western United States and boundary conditions for the NeoKinema model. Boundaries marked as "free*" are not completely free because local velocities are still required to closely match those of local GPS benchmarks.

most compressive horizontal stress azimuths (assumed to be parallel to principal directions of permanent strain between faults), in which $\underline{\sigma_n}$ are their standard errors. There is also a penalty term of the square of a scalar measure (second invariant) of the permanent strain-rate tensor in all unfaulted continuum; in this term, $\underline{r_n}$ is uniformly zero, and $\underline{\sigma_n}$ is the (uniform) model uncertainty in nominally zero permanent continuum strain rates, also known as NeoKinema model parameter μ. The second and third terms are integrated over fault-trace length and crustal surface area, respectively.

Quadratic terms in equation (1) involving fault offset rate estimates are multiplied by an additional weighting factor of (L_m/L_0), in which $L_m = \int_{\text{length}(m)} dl$ is the length of the fault trace for the mth finite element, and L_0 is a model control parameter with units of length. Also, quadratic terms involving continuum strain rate estimates and their principal axis azimuth are multiplied by an additional weighting factor of (A_n/A_0), in which $A_n = \iint_{\text{area}(n)} da$ is the area of the nth finite element, and A_0 is a model control parameter with units of area. Point data at geodetic benchmarks have multipliers of unity. These extra weighting terms could be called "element-discounting weights" because their purpose is to make the objective function (and the eventual solution) independent of the number and size of finite elements used in the grid. Parameters L_0 and A_0 can be adjusted to balance the fit to different classes of data.

NeoKinema was used for the last round of the NSHM and the UCERF3 models in 2014. This round of the NeoKinema update is based on the NSHM2014 model; therefore, all the model setup and parameters from the last round are examined and updated if necessary. The finite-element grid of the revised model for NSHM2023 is shown in Figure 3 and is compared with the updated geological fault distribution. Although new faults have been added in this round of update, most of them have slow (usually ≤1 mm/yr) slip rates, and no change of the model grid is needed for these faults. Two new changes for the grid are (1) a new fault corridor introduced along the Clark segment of the San Jacinto fault to accommodate its fast slip rate, and (2) the fault corridor for the Coachella segment of the San Andreas fault adjusted to fit the new trace of the fault. The rest of the finite-element grid remains the same.

NeoKinema can also use tectonic stress orientation data as model constraints for horizontal strain rate orientations in unfaulted elements. The data set used for the NSHM2014 model worked well, and there is no new information to be added for this round. We therefore use that data set for this model update. We use interpolated, not the original stress orientation, data for

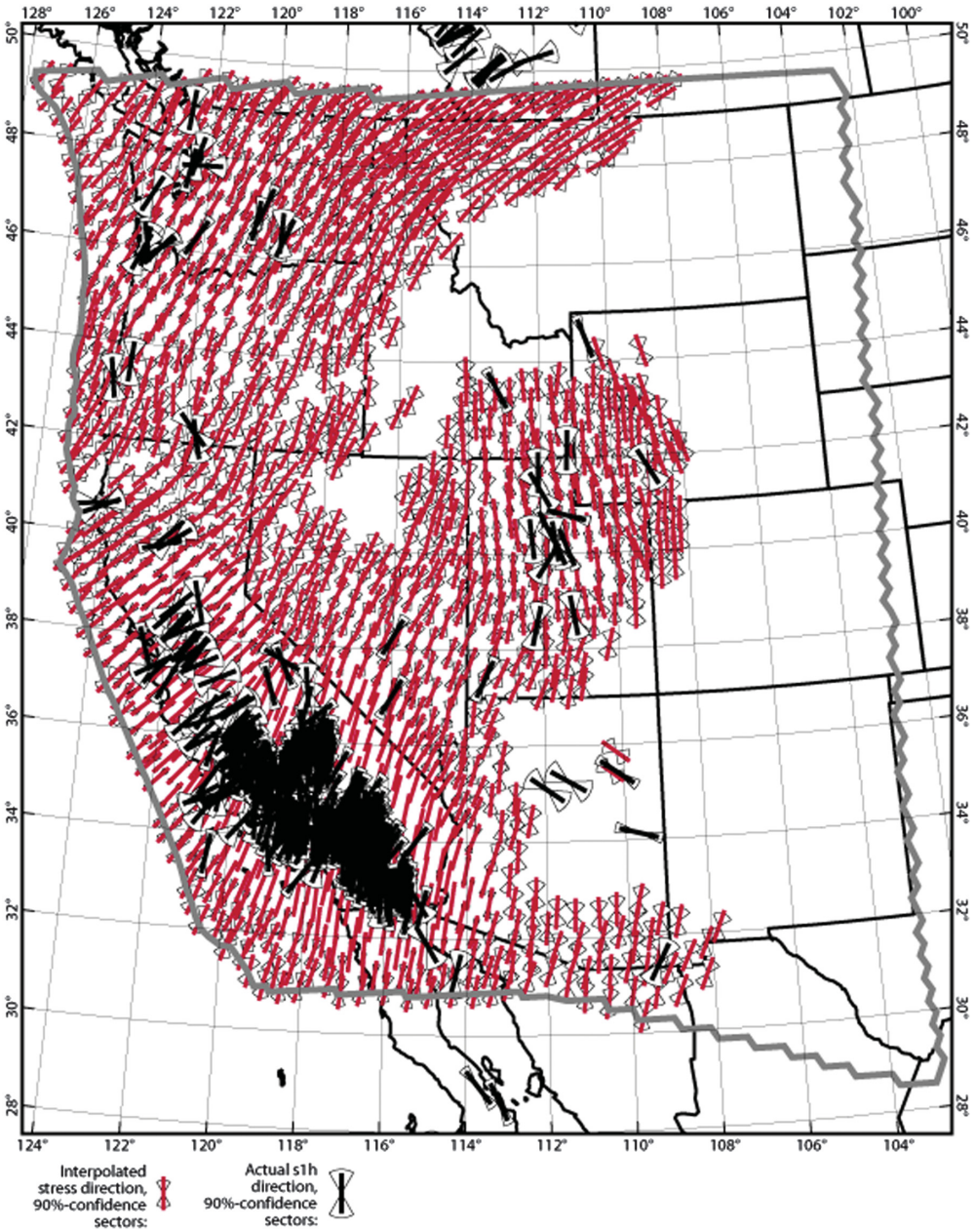

Figure 4. Azimuth of most compressive horizontal principal stress axis. Black and red bars denote raw data and interpolated results, respectively. In areas where no red bars appear, the uncertainty on the interpolated directions was greater than ±45°, and in such places no stress direction constraint was applied.

two reasons: (1) Original data are available for only a small fraction of the finite elements, and if we restricted their influence to only these elements, model results would be too dependent on finite-element sizes. However, interpolated stress directions are available almost everywhere. (2) Most original stress-direction data either lack uncertainties or have ad hoc uncertainties attached (by an unclear process). In contrast, the stress-direction-interpolation method of Bird and Li (1996) that we use provides a quantitative, defensible uncertainty at each point. The data and their interpolation are shown in Figure 4.

We run a series of test models of western U.S. crustal deformation. A set of parameters that remains constant during the test runs is listed in Table S3. Data weighting parameters L_0 and A_0 are varied to search for their optimal combination by examining the normalized postfit residual variance of the data sets. Table 1 lists the normalized postfit residual variance for the three data sets: the stress (equal to strain rate) orientations, potency weighted geological fault-slip rates, and GPS velocities. As shown in Table 1, the data fitting trades off among the three data sets, and the optimal model is determined with the weighting parameters $L_0 = 4 \times 10^8$ m and $A_0 = 2 \times 10^5$ m^2. All the normalized postfit residual variance are <2, indicating that the data fittings are in a reasonable range. The a priori anelastic strain rates in continuum is provided as 5.0×10^{-16}/s, which is between the postfit estimates of the mean continuum strain rate (2.1×10^{-16}/s) and root mean square of continuum strain rate (5.9×10^{-16}/s), and seems to be a reasonable assignment (Bird, 2009).

Figure 5a shows the fault offset rates of the preferred model and the GPS data postfit residuals for western United States, and Figure 5b shows the same but focuses on the southwestern United States. The GPS data postfit residuals are listed in Table S1. Table S4 lists the strike-slip and dip-slip components of the fault offset rate solutions, in which dip-slip is represented by either the relative-vertical velocity component (T or N) or the trace-perpendicular heave rate component (P or D). Fault-slip rates (combining strike-slip and dip-slip) and rakes are listed in Table S5. As can be seen in Figure 5a,b, the highest fault offset rates are along the San Andreas, with 18.0 mm/yr on the North Coast, 19.4 mm/yr on the Santa Cruz Mountains, 28.4 mm/yr on the Creeping, 26.4 mm/yr on the Cholame, 22.2 mm/yr on the Carrizo, 24.2 mm/yr on the

TABLE 1
Postfit Residual Variance of Individual Data Sets

$A_0(10^4\ m^2)/L_0(10^8\ m)$	0.25	0.5	1	2	4	8	12
0.5	/	/	/	1.390*	1.419*	/	/
				1.731*	2.061*†		
				2.249*†	2.213*†		
1.0	/	1.686*	1.616*	1.625	1.587	1.611*	/
		1.559*	1.588*	1.586	1.785	2.179*†	
		2.176*†	2.065*†	1.987	1.946	1.926*	
1.5	/	1.831	1.762	1.764	1.746	1.770	/
		1.532	1.549	1.632	1.648	2.012†	
		2.027†	1.926	1.858	1.810	1.799	
2.0	2.042†	1.952	1.835	1.876	**1.887**	1.834	1.841*
	1.624	1.558	1.544	1.606	**1.583**	1.821	2.096*†
	2.035†	1.921	1.834	1.776	**1.732**	1.705	1.697*
2.5	/	2.050†	1.936	1.940	1.987	1.919	1.942
		1.572	1.529	1.574	1.576	1.729	1.945
		1.849	1.766	1.710	1.674	1.646	1.634
3.0	/	/	2.034†	2.025†	2.081†	2.033†	2.019†
			1.523	1.569	1.673	1.676	1.862
			1.712	1.663	1.626	1.602	1.586

L_0 is equivalent to the length of fault trace whose slip rate gets unit weight (in m), and A_0 is equivalent to the area of continuum whose stiffness and isotropy get unit weight (in m^2). Both are relative to a weight of unity for a Global Positioning System [GPS] benchmark.
The top, middle, and bottom numbers in each entry are the normalized postfit residual variance for the stress orientation, potency weighted geological fault offset rate, and GPS velocity data, respectively. The group of three residual variances marked in bold font is the preferred solution.
*The solutions with at least one postfit residual variance >2.05 and are not included in the uncertainty estimation.
†Marginal solutions whose postfit residual variance are ~2.0.

Mojave, 18.4 mm/yr on the Northern San Bernardino, and 15.2 mm/yr on the Coachella segments, respectively. The offset rates are 14.4 mm/yr on the Imperial, 9.9 mm/yr on the Hayward, 14.9 mm/yr on the Calaveras, 7.7 mm/yr on the Rodgers Creek, and 4.4 mm/yr on the Garlock faults, respectively. We compute the total seismic moment rate on fault as $\dot{M} = \sum_1^n \int G w_i s_i dl_i$, in which w is the width of the seismogenic part of the fault, s is the fault-slip rate, G is the shear modulus of the brittle crust (assumed 30 GPa), l is the trace length of seismogenic portion of the trace, and i is the sequential number of the fault. The result yields $\dot{M} = 2.572 \times 10^{19}\ \mathrm{N \cdot m/yr}$. Recall that this on-fault seismic moment rate does not include the megathrust of the Cascadia subduction zone.

Figure 6 plots the long-term strain rates in the western United States, which seem to be broadly distributed. The strain rates are in the order of $\sim 10^{-14}$/s in the vicinity of some fast slipping faults in California and western Nevada, $\sim 10^{-15}$/s in most part of California, Nevada, Cascadia subduction zone, and the Yellowstone–Wasatch fault region, and $\sim 10^{-16}$–10^{-17}/s in other parts of the western United States west of 104° W. Assuming that the off-fault seismic moment $\dot{M}_{\mathrm{off-fault}} = \iint_{\mathrm{area}} G\langle cz\rangle k\varepsilon_{\mathrm{great}} da$. Here, $\langle cz\rangle$ is the coupled thickness of seismogenic lithosphere from table 5 of Bird and Kagan (2004); for example, 8.6 km in a continental strike-slip setting. G = 30 GPa is the shear modulus, and k and $\varepsilon_{\mathrm{great}}$ are strain-rate factors defined in the appendix of Carafa *et al.* (2017). With this formulation, our model yields $\dot{M}_{\mathrm{off-fault}} = 8.685 \times 10^{18}\ \mathrm{N \cdot m/yr}$. Recall that this figure does not include any plate-bending earthquakes that might occur in the Juan de Fuca plate that is subducting at the Cascadia subduction zone.

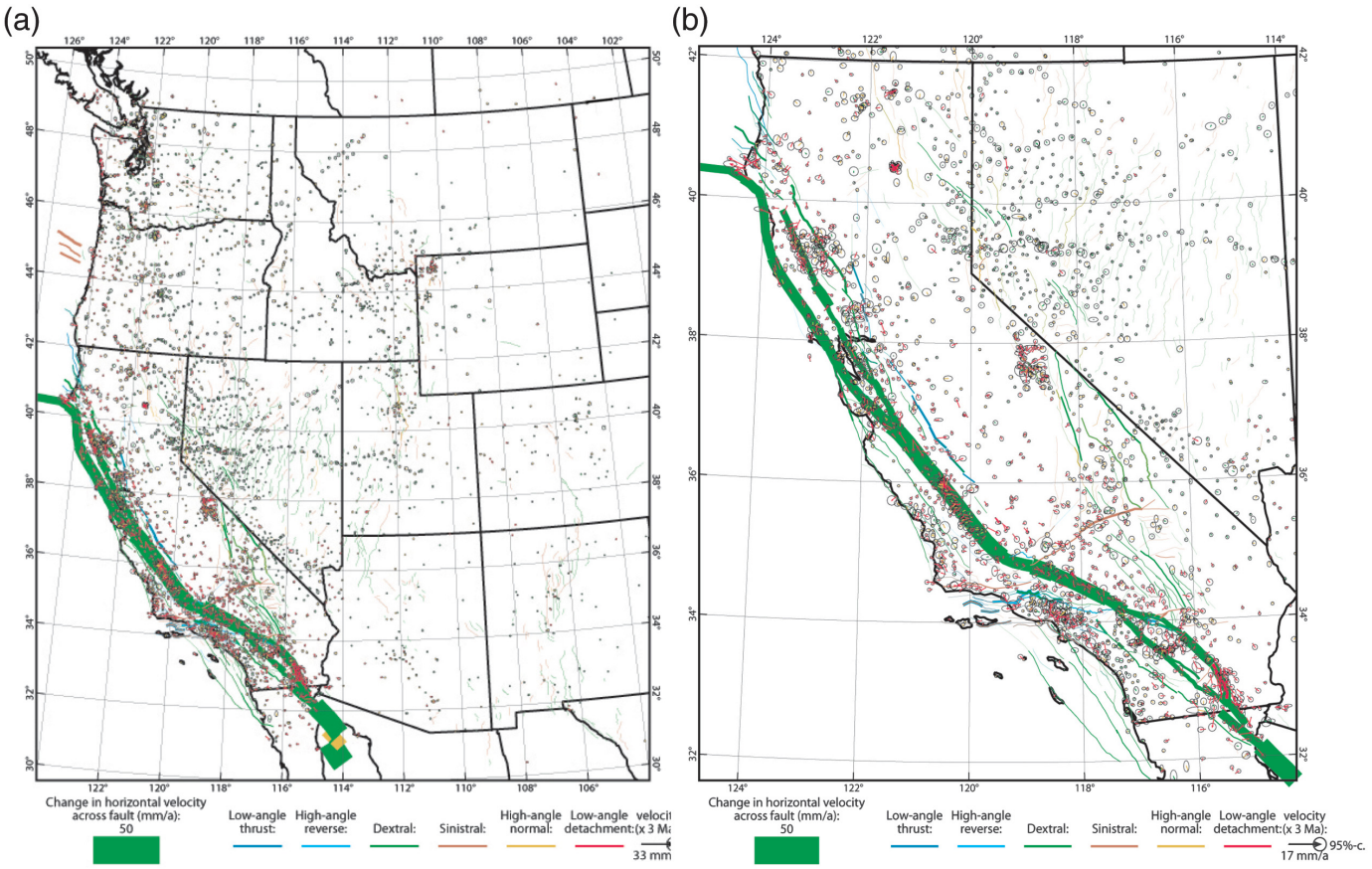

Figure 5. Western U.S. horizontal fault offset rates and GPS velocity postfit residuals. This solution is for the optimal model identified by residuals in bold font in Table 1. (a) Western U.S. area. (b) Southwest U.S. area.

Discussion

Validity of geological fault-slip rate bounds

One controversial aspect of the NSHM program is that the geologic fault-slip rates provided as input for deformation modeling are a mixture of two types: scientific data and opinions. The better fault offset rates are based on the separation of offset features (pairs of piercing points or piercing planes) divided by the measured age of the offset feature. Such data can be treated statistically (e.g., Bird, 2007) to estimate the probability density function for the offset rate. Because some faults display more than one pair of offset features, it is even possible to estimate the fraction of apparent offset pairs that are erroneous: Bird (2007) estimated this as 4% to ~5% for Quaternary features in the western United States. However, such data are only available for a minority of the faults that are to be modeled.

In other cases, the geologist assigned to review all available information on the fault is charged with making an assignment of its offset rate to a standard bin: <0.2, 0.2–1, 1–5, or >5 mm/yr. Factors considered might include apparent (subjective) age of units cut or not cut along the trace, prominence of the scarp, nearby seismicity, and geometric relation to other faults of known rate. Although such considerations are relevant and useful, their combination is inherently subjective and nonreproducible.

In cases in which the rate-bin assignment is correct, it helps the deformation model by limiting the possible error in fault-slip rate to the width of the bin, at worst. But where the rate-bin assignment is incorrect, it would enforce a minimum error in fault-slip rate, and potentially contaminate the modeling of other faults nearby. Therefore, an important question is, how often are these subjective rate-bin assignments correct?

In this project, we chose to conduct our NeoKinema modeling with looser rate bounds, ranging from 75% of the USGS lower bound rate (r_{min}) to 125% of the USGS upper bound rate (r_{max}). We then took the rates predicted by the preferred NeoKinema model (p) and converted them to the nondimensional relative measure $s = (p - r_{min})/(r_{max} - r_{min})$. The distribution of s is shown as a histogram in Figure 7. This figure shows a distribution that is not very different from Gaussian but wider than the USGS bounds; about 20% of the NeoKinema model rates fell outside them. Therefore, we advocate for a similar loose enforcement of these bounds in future modeling. If we had enforced them literally, the resulting histogram would have been W-shaped rather than Gaussian, with two artificial peaks occurring at the lower and the upper bound, respectively.

On-fault and off-fault seismic moment rates

One important innovation in the NSHM modeling process this year is to compute model maps of "off-fault" rates of permanent

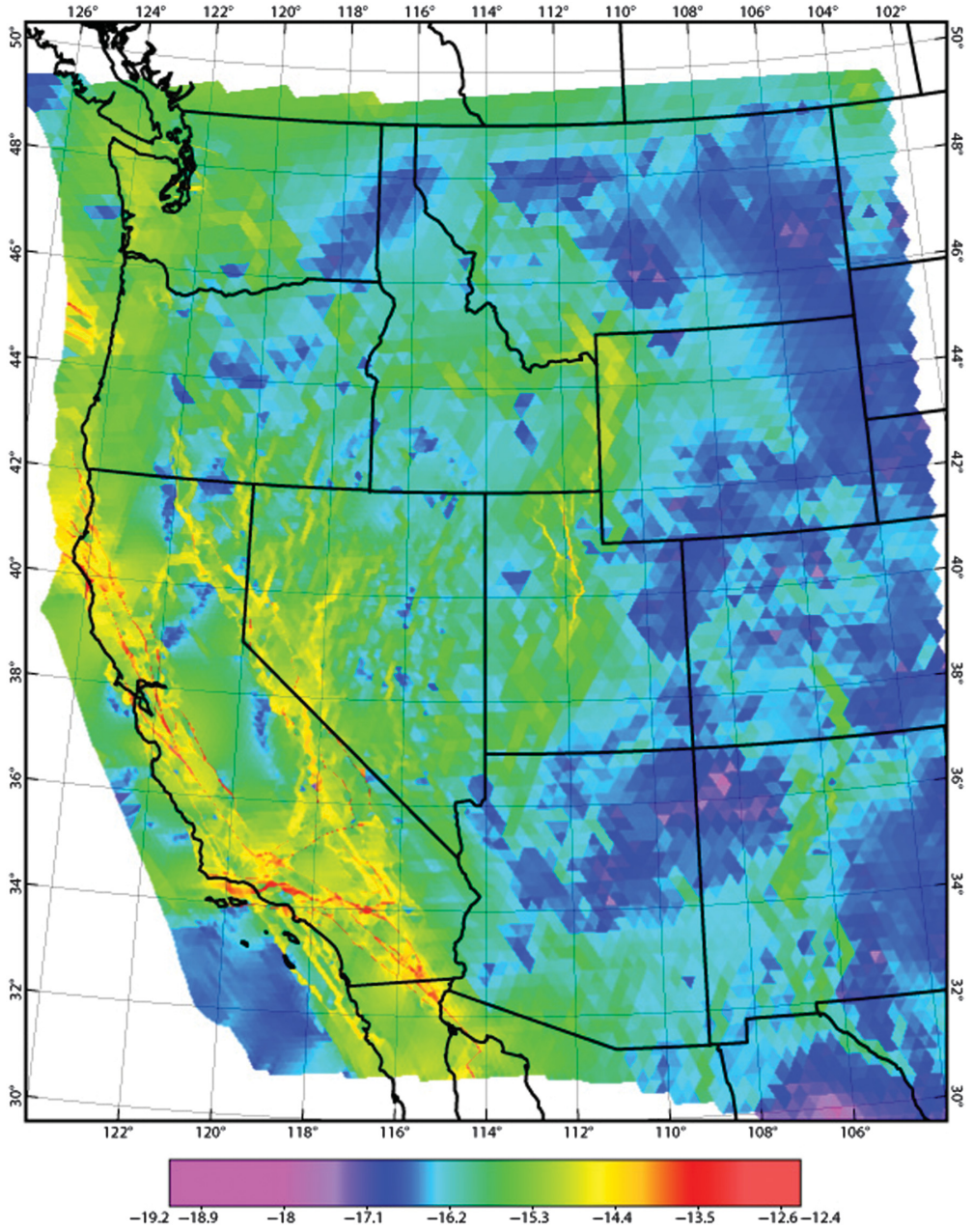

Figure 6. Western U.S. long-term strain rates (including both coseismic and interseismic). The specific magnitudes shown along faults are equivalent to fault offset rates divided by "fault corridor" widths; thus, they include a factor that is model dependent.

(nonelastic) deformation and incorporate their implied seismic moment rates and seismicities into the seismic hazard. Unfortunately, little is known about how much of this off-fault deformation is seismogenic. Our estimates here are based on the set of assumptions and approximations known as the Seismic Hazard Inferred from Tectonics (SHIFT) method of Bird and Liu (2007), which rests on the global plate-tectonic seismicity calibration of Bird and Kagan (2004). By this method, the estimated total seismic moment rate of the model area (excluding the Cascadia subduction zone) is 3.44×10^{19} N · m/yr, of which 2.57×10^{19} (74.7%) is generated on modeled faults, and 8.69×10^{18} (25.3%) is generated in the continuum between the modeled faults. This proportion seems reasonable in light of the previous estimate of Bird (2009) that one-third of PA-NA relative plate motion in the latitude of California is accommodated by distributed permanent strain between modeled faults. Some other authors have produced alternative deformation models that give similar proportions (Johnson, 2013; Parsons *et al.*, 2013; Zeng and Shen, 2016; Hearn, 2019). Now, the SHIFT method utilizes a coupled lithosphere thickness $<cz>=8.6$km in continental strike-slip zones, which are dominant in this model. Another plausible approach would be to adopt a higher $\langle cz \rangle = 15$ km based on the maximum hypocenter depth $z = 15$ km inferred by Nazareth and Hauksson (2004) and an assumption of perfect coupling ($c = 1$). In that case, the off-fault seismic moment rate could increase by a factor of about (15/8.6) = 1.74, the off-fault seismic moment rate would rise to about 1.5×10^{19} N · m/yr, and the off-fault contribution to the total seismic moment rate would increase to about 37%. Continuing research is needed on the effective seismic coupling of "off-fault" (or "off-modeled-fault") regions in the crust.

Fault-slip rate uncertainty estimate

Although data uncertainties are provided for NeoKinema's data input, NeoKinema does not include any algebraic pathway to map the data uncertainties into solution uncertainties. The solution uncertainties, however, may be assessed through evaluating solutions with different data weighting. Table 1 lists statistics of data postfit residual variance employing different weighting parameters L_0 and A_0. Taking all the solutions whose weighted postfit residual variance for the three data

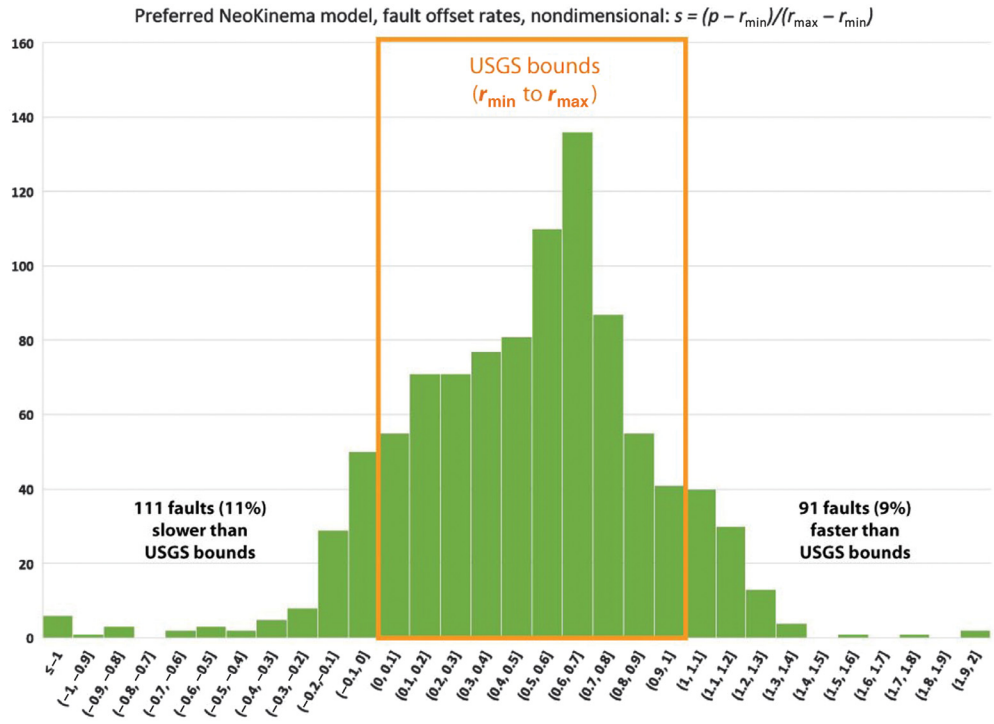

Figure 7. Histogram of fault slip rates as function of the nondimensional relative measure *s*.

sets are less than 2.05, we can obtain the range of acceptable offset-rate solutions S_r for each fault segment and assign its uncertainty $\sigma = 0.5S_r$. The uncertainties determined in this way provide an assessment of the level of constraint the data impose on the solution and are listed in Table S5 along with the fault offset-rate estimates.

Comparison with geological fault offset rates

We plot the fault offset-rate estimates of our preferred model against the preferred geological offset rates (both data sets are listed in Table S6) and find that, although the two are consistent overall, our estimates for the faults with higher slip rates tend to be slower than the preferred geological rates (Fig. 8c). The largest discrepancies are for a group of San Andreas fault segments: the Carrizo (discrepancy 7.1 mm/yr), Cholame (6.5 mm/yr), Big Bend (14.5 mm/yr), Mojave (5.4 mm/yr), Offshore (7.9 mm/yr), and Brawley (7.7 mm/yr). Other faults with large discrepancies include the Hayward South Extension (7.7 mm/yr), Mendocino (6.0 mm/yr), and West Garlock (5.9 mm/yr). The only large discrepancy in which our estimate is greater than the geological rate is the Cerro Prieto fault (9.7 mm/yr).

We also ran a solution without imposing the ghost transient deformation correction to GPS data, to investigate its possible impact on the solution. The normalized data postfit residual variances are 1.638 for stress orientation, 1.765 for geological fault offset rate, and 1.664 for GPS velocity data. We find that data fitting for the model with the ghost transient correction is slightly worse for stress orientation and for GPS velocity data, but better for geological slip rates. Figure 8c demonstrates that the fault offset rate estimates for the case with ghost transient correction are indeed closer to geological estimates than those without such a correction, particularly for faults with large offset rates. We conclude that including this correction improves model fitting to geological data.

Comparison with 2014 NeoKinema NSHM solution

We also compare the current solution with the 2014 NeoKinema NSHM solution version 3.2 (Neok2014). Figure 9a plots pairs of slip rates of the two solutions for the same fault segments (the data are listed in Table S6). Only fault segments with geological slip rates >5 mm/yr are shown. The two solutions are in good agreement overall, but deviations are also evident that are on the order of a few millimeters per year. The overall trend is that the Neok2014 estimates were slightly slower than those in this new solution. Part of this change may be explained by the transient deformation caused by viscous postseismic relaxation following large earthquakes, whose effect is corrected in this solution but not in Neok2014.

Figure 9b shows locations of faults with large offset-rate ratios between this study and Neok2014. The ones with significant offset rates (>5 mm/yr) and the ratio of (slip rate from this study)/(slip rate from Neok2014) > 3 include Pita Point, Superstition Hills, Hayward South Extension, San Andreas (North Branch Mill Creek), and Rogers Creek faults. The major rate increase on the North Branch Mill Creek segment of the San Andreas reflects new interpretations of the field geology (Blisniuk *et al.*, 2021) since the previous NSHM project. The faults with significant offset rates (>5 mm/yr) and a low value of the same ratio, <1/3, include Eureka Peak, Hector Mine, and West Garlock faults. The higher Neok2014 rates in these latter cases may have resulted from using GPS velocities that contained postseismic signals of the 1992 Landers and 1999 Hector Mine earthquakes in the Mojave shear zone region.

Long-term seismicity forecast

Using the fault offset rates from our preferred model, together with the tensor rates of permanent strain in the unfaulted

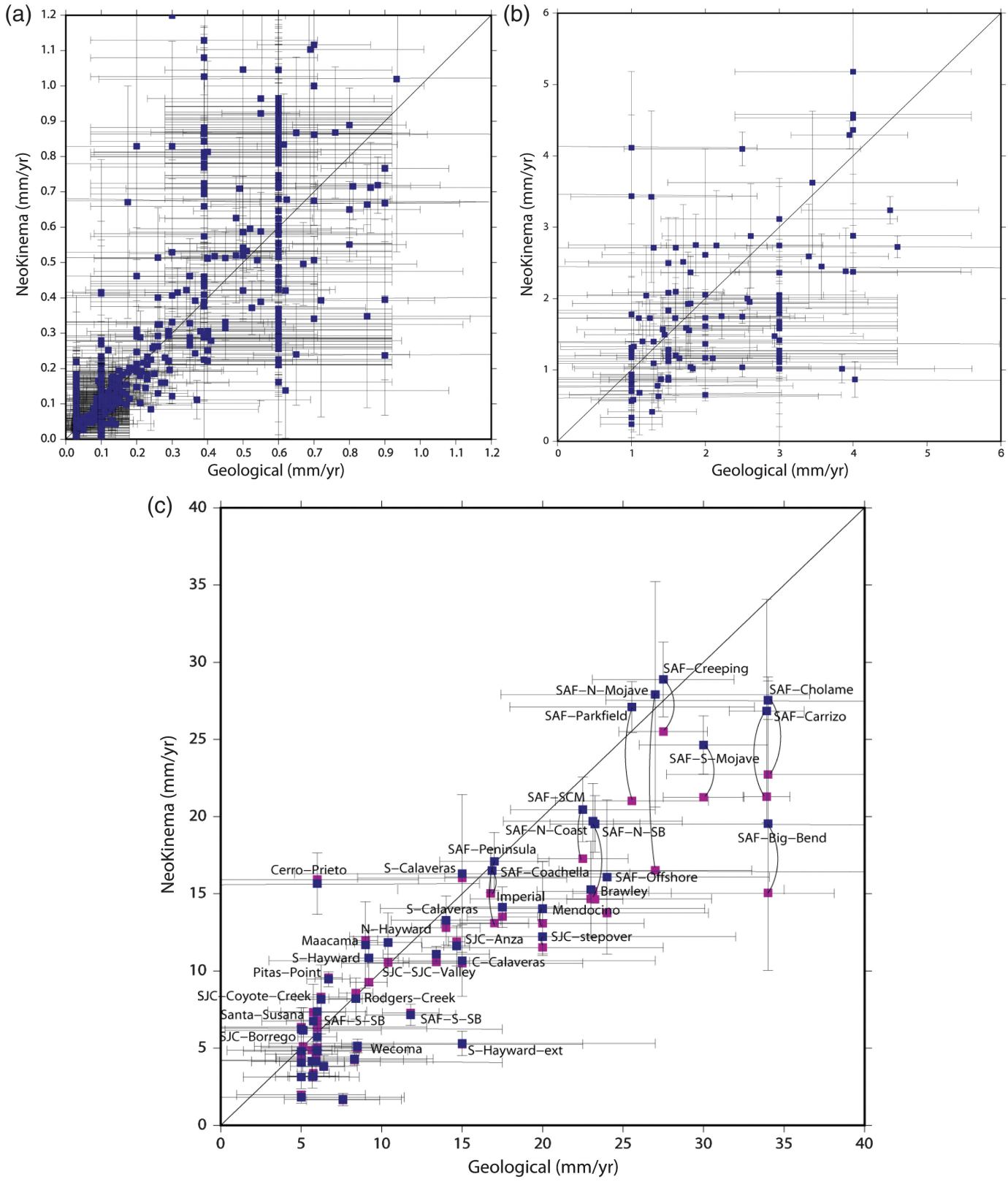

Figure 8. Comparison of fault offset rates from our preferred model with preferred geologic offset rates (blue squares). Panels (a), (b), and (c) are for data ranges of 0–1, 1–5, and 5–35 mm/yr, respectively. Purple squares in panel (c) show our model result without the ghost transient correction to GPS velocities, whereas connected blue squares show our model with the ghost transient correction.

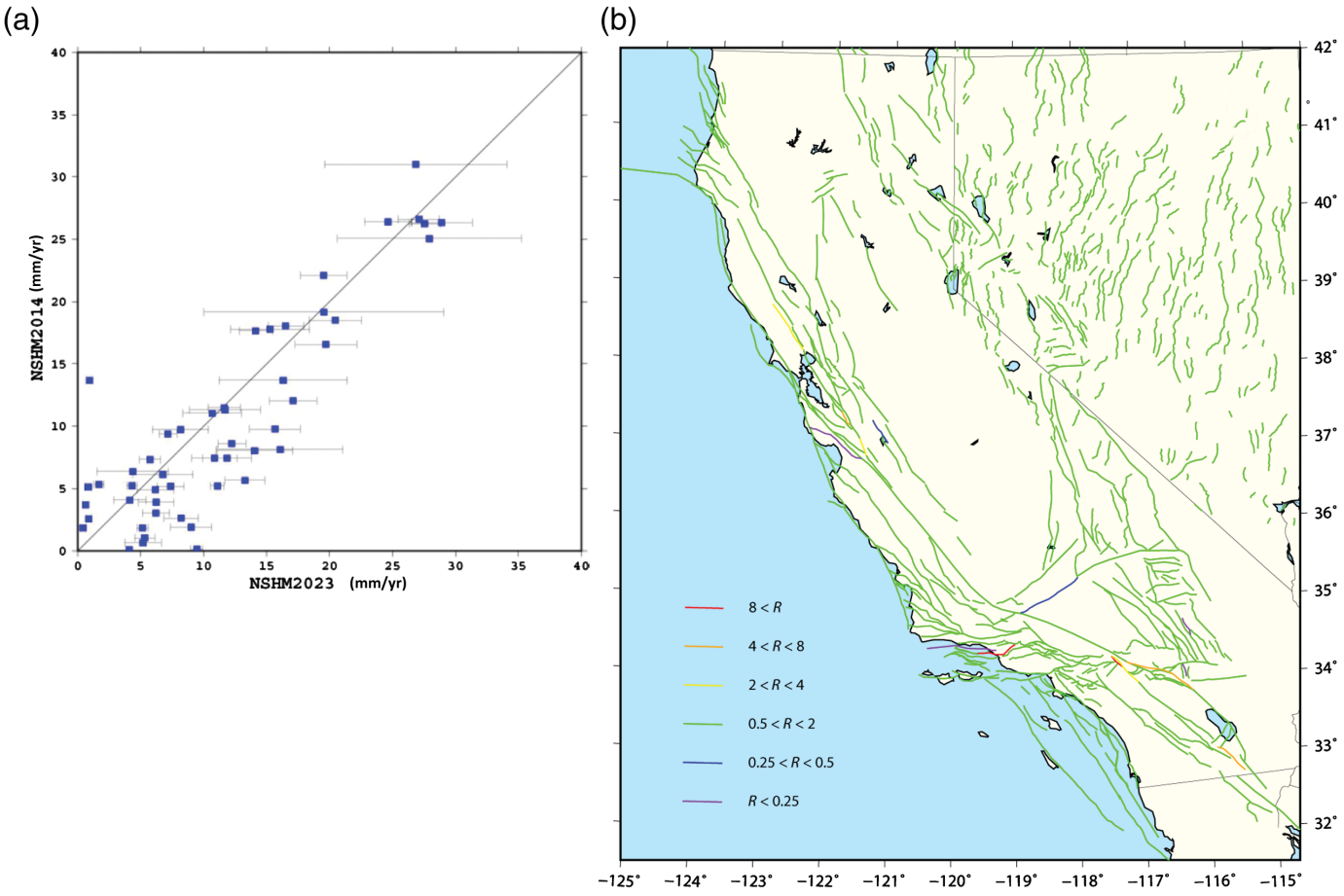

Figure 9. (a) Comparison of fault-slip rates between this study and NeoKinema NSHM2014 model version 3.2. (The largest discrepancy, 1 vs. 14 mm/yr, is from the Eureka Peak fault, located in the eastern Transverse ranges and south of the Pinto Mountain fault.) (b) Fault offset rate ratios. R = rate (this study)/rate (NSHM2014): $R < 0.25$, purple; $0.25 < R < 0.5$, blue; $0.5 < R < 2$, green; $2 < R < 4$, yellow; $4 < R < 8$, orange; $8 < R$, red.

continuum, we also compute a long-term forecast of shallow seismicity for the conterminous western United States. We use version 11 of the code Long_Term_Seismicity. This code implements the SHIFT hypotheses as developed over a number of studies (Bird and Liu, 2007; Bird *et al.*, 2009; Bird *et al.*, 2010; Bird and Kreemer, 2015a,b; Carafa *et al.*, 2017), with calibration of coupled lithosphere thicknesses $\langle cz \rangle$ and corner magnitudes and spectral slopes all taken from the global calibration study of Bird and Kagan (2004), which in turn made use of the PB2002 plate boundary model (Bird, 2003).

The irregularly shaped domain of the finite-element grid in this study could lead to two problems in this seismicity forecast: (1) It would exclude much of the seismicity expected to result from Juan de Fuca–North America plate interaction at (or near) the Cascadia subduction zone; and (2) the shape of the domain would not be acceptable input for many standard programs that quantitatively test and rank seismicity forecasts. For both reasons, code Long_Term_Seismicity uses supplemental models to fill in the edges of a trapezoidal forecast region that is "rectangular" in terms of its (longitude, latitude) limits. The positions of the Cascadia megathrust trace and the Gulf of California transtensional boundary and their relative plate velocities are taken from PB2002 (Bird, 2003), with forecast seismicity spread about the trace of both plate boundaries according to empirical spatial-footprint functions obtained by Bird and Kagan (2004). The very small permanent strain rates expected in the offshore portions of the Pacific plate are from the preferred Shells dynamic model Earth5-049 of Bird *et al.* (2008). The final result is a seismicity rate forecast of shallow (≤70 km) hypocentroids with moment magnitudes of $M_w > 5.663$, which is plotted in Figure 10. As can be seen, the seismicity forecast mimics the long-term deformation pattern shown in Figure 6, and the highest seismicity rates come from the San Andreas fault system and the Cascadia subduction zone. Nevertheless significant seismicity rates also concentrate along the eastern California shear zone and Walker Lane faults, and along the Wasatch fault system. The off-fault seismicity is broadly distributed, particularly around the Cascadia subduction zone (where it reflects expected plate-bending seismicity in the Juan de Fuca plate) and the Gulf of California plate-boundary zone, neither of which is included as a fault source in this study, and their seismogenic deformation is regarded as off-fault deformation and seismicity

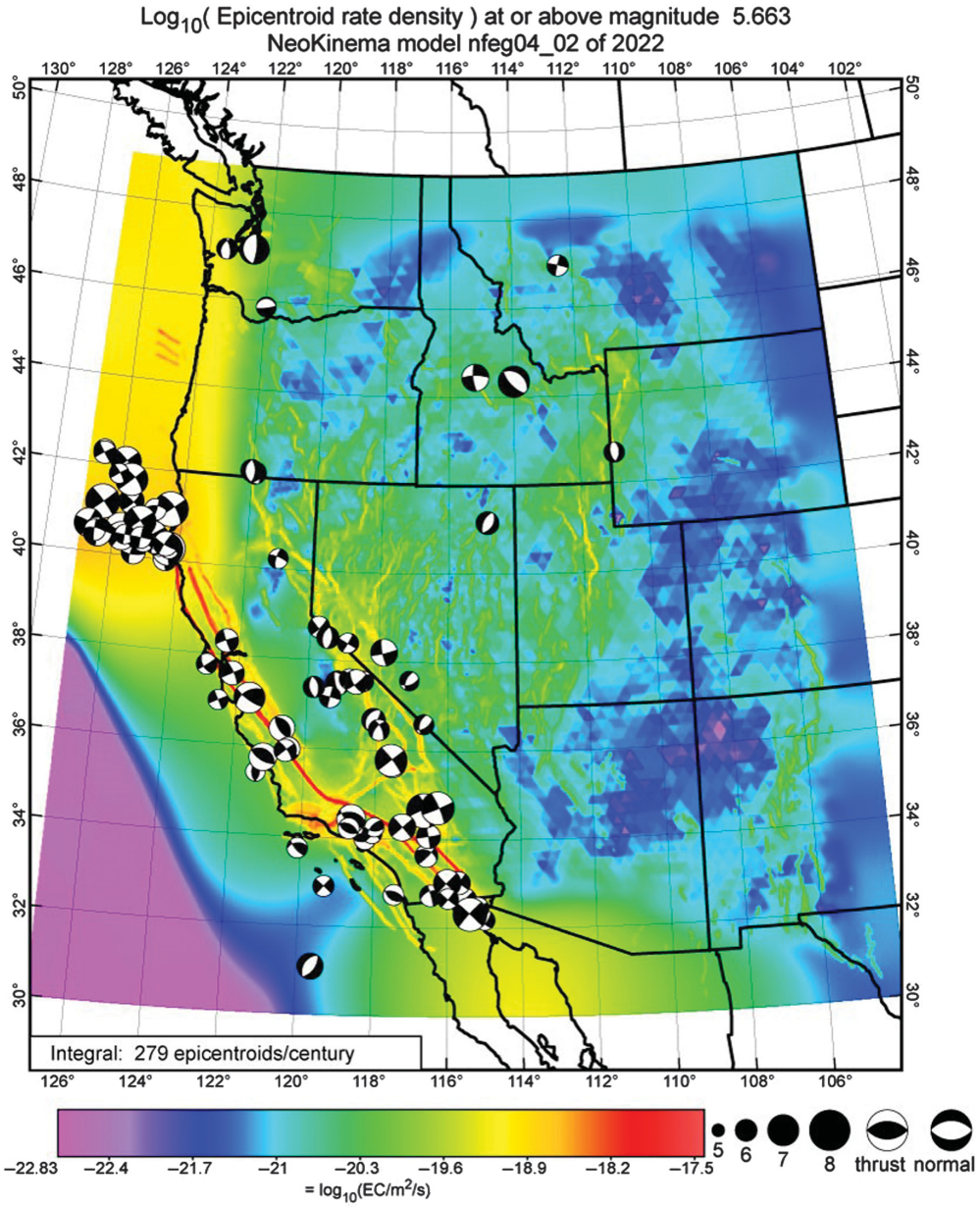

Figure 10. Long-term seismicity forecast and Global Centroid Moment Tensor earthquake catalog 1977–2021 for events $M_w > 5.663$.

in the model. The total seismicity rate is 2.78 events/yr, which breaks down as 56.8% on fault and 43.2% off-fault. These proportions do include the contributions from Cascadia, unlike the proportions quoted earlier for the NeoKinema model domain alone. The expected high "off-fault" seismicity (due to plate-bending) in the slow Cascadia subduction zone raises the regional "off-fault" proportion above the value that we found previously in land areas of western North America.

Retrospective evaluation of seismicity forecast

Our seismicity forecast is entirely based upon tectonic deformation rates and makes no use of smoothed seismicity. Thus, it is independent of local earthquake catalogs. This makes it possible to compare the forecast to any existing catalog that is accurate and complete. Here, we use the Global Centroid Moment Tensor (Global CMT) catalog (see Data and Resources for the source), selecting hypocentral depths no deeper than 70 km, and magnitudes of 5.663 or higher (scalar moment 3.5×10^{17} N · m or higher), in the years 1977–2021.

The count of Global CMT hypocenters meeting these criteria is 91. However, over any 45 yr period, our forecast would imply an expectation of 125 events. Theoretically, if seismicity were Poissonian in time, then the expected standard deviation of the expectation of 125 would be its square root, or 11.2. Therefore, this discrepancy would amount to 3.0 standard deviations, and would be significant.

There are two basic hypotheses to explain this: (A) Our seismicity forecast is biased high by some systematic error; or (B) the seismicity of the western United States has been below its long-term average (by about 27%) during the last 45 yr. The latter can be expanded into sub-hypotheses suggesting possible reasons: (B1) Because real seismicity is clustered rather than Poissonian, the fraction of time windows that have event counts less than the long-term mean is much higher than 50%, and such discrepancies are not unusual; and/or (B2) seismicity has been low because of the lingering stress shadows following the great Cascadia earthquake of A.D. 1700 and the San Andreas earthquakes of 1857 and 1906; and/or (B3) seismicity has been temporarily depressed because the upper crust is strengthened by falling water tables resulting from both groundwater mining and long-term droughts induced by climate change. These hypotheses are not mutually exclusive and could be complementary.

Clearly it is important to begin by evaluating hypothesis (A) of model bias, because only this hypothesis would support

seismic hazard forecasts based on continuation of the seismicity level of the last 45 yr. A good step toward a test of (A) would be to convert all other competing deformation models to long-term seismicity forecasts for the same map-window and threshold magnitude and then compare their rates.

We can also evaluate the forecast for the quality of its predicted spatial map. Two good tools are the I_0 and I_1 information scores (Kagan, 2009; Bird, 2018). The I_0 ("specificity") score is computed from the forecast map alone and rates how informative it is: our model gives $I_0 = 2.56$. The I_1 ("success") score also considers a test catalog (here, Global CMT 1977–2021) and rates how well the seismicity matches the forecast: our model gives $I_1 = 1.17$. (Both measures are in units of binary bits of information gain relative to a spatially uniform forecast.) We find $I_1 < I_0$ because of the big spatial discrepancy in the northwest corner of the map (Fig. 10), in which the Cascadia subduction zone has been strangely silent in the last 45 yr.

Another useful metric is the likelihood-based *S*-statistic (Schorlemmer *et al.*, 2007). A large number of virtual earthquake catalogs are generated from the forecast, each with the same number of events as the actual test catalog. Then, all catalogs (real and virtual) have their likelihoods computed, based on a temporary hypothesis that the forecast is correct. The *S*-statistic is the fraction of virtual catalogs that have likelihoods lower than the actual catalog. A value of 0.5 is ideal, meaning that likelihood alone cannot distinguish the forecast from reality. A value much less than 0.5 means that the forecast map has spatial deficiencies. Our result is $S = 0.069$, which is low but does not reject the forecast (with 95% confidence).

A third metric is the area skill score of Zechar and Jordan (2008). Our model results in a statistic of 0.865 (relative to an ideal of 1.0), showing that it is significantly better than a spatially uniform forecast but far from ideal.

It is difficult to evaluate such scores in isolation. If all other competing deformation models of the same region were converted to long-term seismicity forecasts and scored in parallel, we could obtain more meaningful relative ranks. Still, doubt would remain about whether the recent 45 yr instrumental time window is enough of a basis for choosing among models that have many other good attributes. The behavior of Cascadia suggests that at least 400 yr of catalog would be needed to do this reliably, based on seismicity alone.

Conclusions

Our modeling of long-term neotectonics in the western United States with NeoKinema was successful, according to three criteria: (1) The postfit residual variances for GPS data, geologic slip rates, and stress directions were reduced to 1.732, 1.583, and 1.887, respectively. (2) Postfit residual GPS velocities at the benchmarks used in modeling were spatially scattered, not indicating any particular problem areas. (3) Changes in predicted fault-slip rates from the NeoKinema models of the previous NSHM update were mostly in the direction of better matching to geologic rates, mainly due to the incorporation of the ghost-transient correction to GPS velocities.

An important caveat is that such good matching of GPS velocities was only achieved after careful editing and correction of these data. As detailed earlier, benchmarks in narrow "fault corridors" of our finite-element grid were omitted; multiple velocity solutions for the same benchmark (due to subtle differences in velocity reference frame) were merged; benchmarks showing locally or temporally anomalous velocity due to nonsteady tectonics (e.g., volcanism or time-dependent fault creep) were omitted; all remaining benchmarks had velocities corrected to remove elastic strain accumulation in Cascadia, and all remaining benchmarks had their velocities corrected from decade-specific to long-term-average-interseismic by use of the ghost-transient correction.

Similarly, we examined the geologic slip-rate data set provided and raised a question about the reliability of slip-rate-bin assignments for faults that lack dated offset features. Without changing these input goals or their standard errors, we permitted our code to find slip rates ranging from 75% of the geologic lower bound to 125% of the geologic upper bound. The result was that about 20% of faults had computed slip rates outside their nominal bounds, but the histogram of nondimensionalized slip rates (relative to the original bounding range) was converted to a near-Gaussian distribution, without any clustering at the rate boundaries.

Our model predicts a significant amount of "off-fault deformation," meaning nonelastic permanent deformation that occurs between the modeled fault traces. This is important because it is at least partially seismogenic. In the area of our finite-element grid (therefore excluding much of the Cascadia subduction zone), we compute an "off-fault" seismic moment rate that is 25% of the regional total. If there were complete seismic coupling of this off-fault deformation, the off-fault seismic moment rate could be as high as 37% of a greater total. Thus, the computed map of off-fault permanent deformation rates is an important contribution to the deformation-modeling effort.

Finally, we used the tools developed based on the SHIFT hypotheses to compute a tentative map of long-term seismicity for the region. The spatial-integral of this map indicates a predicted long-term seismicity rate that is 27% higher than the rate recorded in the Global CMT catalog for 1977–2021. We attribute this to the fact that most of the Cascadia subduction zone has been extremely quiet for the last 45 yr; however, historic and prehistoric great earthquakes there suggest that this quietude will not continue. We compute various metrics of the success of our seismicity forecast map using Global CMT 1977–2021 as the test catalog but have difficulty assessing the meaning of these results given that (1) competing deformation models have not yet been converted to seismicity forecast maps and scored in parallel fashion; and (2) the Global CMT catalog is clearly too short to assess the quality of any long-term seismicity models that include Cascadia.

Data and Resources

The Quaternary Fault and Fold Database of the United States was obtained from https://www.usgs.gov/natural-hazards/earthquake-hazards/faults (last accessed August 2022). The Global Centroid Moment Tensor Project database was searched using www.globalcmt.org/CMTsearch.html (last accessed May 2022). Some plots were made using the Generic Mapping Tools version 4.2.1 (Wessel and Smith, 1998). The fault geometry data and slip rate solutions are provided in the supplemental material.

Declaration of Competing Interests

The authors acknowledge there are no conflicts of interest recorded.

Acknowledgments

The authors are grateful to Tony Lowry, an anonymous reviewer, and Associate Editor Fred Pollitz for their constructive comments that helped improve this article. This research is supported by a grant from the U.S. Geological Survey (G11AP20044). Southern California Earthquake Center Publication Number 12026.

References

Bird, P. (2003). An updated digital model of plate boundaries, *Geochem. Geophys. Geosys.* **4,** no. 3, doi: 10.1029/2001GC000252.

Bird, P. (2007). Uncertainties in long-term geologic offset rates of faults: General principles illustrated with data from California and other western states, *Geosphere* **3,** no. 6, 577–595, doi: 10.1130/GES00127.1.

Bird, P. (2009). Long-term fault slip rates, distributed deformation rates, and forecast of seismicity in the western United States from joint fitting of community geologic, geodetic, and stress direction data sets, *J. Geophys. Res.* **114,** no. B11, doi: 10.1029/2009JB006317.

Bird, P. (2018). Ranking some global forecasts with the Kagan information score, *Seismol. Res. Lett.* **89,** no. 4, 1272–1276, doi: 10.1785/0220180029.

Bird, P., and M. M. Carafa (2016). Improving deformation models by discounting transient signals in geodetic data: 1. Concept and synthetic examples, *J. Geophys. Res.* **121,** no. 7, 5538–5556.

Bird, P., and Y. Y. Kagan (2004). Plate-tectonic analysis of shallow seismicity: Apparent boundary width, beta, corner magnitude, coupled lithosphere thickness, and coupling in seven tectonic settings, *Bull. Seismol. Soc. Am.* **94,** no. 6, 2380–2399.

Bird, P., and C. Kreemer (2015a). Revised tectonic forecast of global shallow seismicity based on version 2.1 of the Global Strain Rate Map, *Bull. Seismol. Soc. Am.* **105,** no. 1, 152–166, doi: 10.1785/0120140129.

Bird, P., and C. Kreemer (2015b). Erratum to "Revised tectonic forecast of global shallow seismicity based on version 2.1 of the Global Strain Rate Map," *Bull. Seismol. Soc. Am.* **105,** no. 3, 1823–1824, doi: 10.1785/0120150068.

Bird, P., and Y. Li (1996). Interpolation of principal stress directions by nonparametric statistics: Global maps with confidence limits, *J. Geophys. Res.* **101,** no. B3, 5435–5443.

Bird, P., and Z. Liu (2007). Seismic hazard inferred from tectonics: California, *Seismol. Res. Lett.* **78,** no. 1, 37–48.

Bird, P., Y. Y. Kagan, D. D. Jackson, F. P. Schoenberg, and M. J. Werner (2009). Linear and nonlinear relations between relative plate velocity and seismicity, *Bull. Seismol. Soc. Am.* **99,** no. 6, 3097–3113, doi: 10.1785/0120090082.

Bird, P., C. Kreemer, and W. E. Holt (2010). A long-term forecast of shallow seismicity based on the Global Strain Rate Map, *Seismol. Res. Lett.* **81,** no. 2, 184–194.

Bird, P., Z. Liu, and W. K. Rucker (2008). Stresses that drive the plates from below: Definitions, computational path, model optimization, and error analysis, *J. Geophys. Res.* **113,** no. B11, doi: 10.1029/2007JB005460.

Blisniuk, K., K. Scharer, W. Sharp, R. Burgmann, C. Amos, and M. Rymer (2021). A revised position for the primary strand of the Pleistocene-Holocene San Andreas fault in southern California, *Sci. Adv.* **7,** no. 13, doi: 10.1126/sciadv.aaz5691.

Carafa, M. M. C., G. Valensise, and P. Bird (2017). Assessing the seismic coupling of shallow continental faults and its impact on seismic hazard estimates: A case-study from Italy, *Geophys. J. Int.* **209,** 32–47, doi: 10.1093/gji/ggx002.

Devries, P. M. R., P. Krastev, J. F. Dolan, and B. J. Meade (2017). Viscoelastic block models of the North Anatolian fault: A unified earthquake cycle representation of pre- and postseismic geodetic observations, *Bull. Seismol. Soc. Am.* **107,** 403–417, doi: 10.1785/0120160059.

Field, E. H., G. P. Biasi, P. Bird, T. E. Dawson, K. R. Felzer, and D. D. Jackson (2013). Uniform California Earthquake Rupture Forecast, Version 3 (UCERF3)—The time-independent model, *U.S. Geol. Surv. Open-File Rept. 2013-1165*.

Hatem, A. E., C. M. Collett, R. W. Briggs, R. D. Gold, S. J. Angster, P. M. Powers, E. Field, H. Anderson, M. Ben-Horin, Y. J. Choi, *et al.* (2022). Earthquake geology inputs for the US National Seismic Hazard Model (NSHM) 2023 (western US) (ver. 2.0, February 2022), *U.S. Geol. Surv. Data Release*, doi: 10.5066/P9AU713N.

Hatem, A. E., N. Reitman, R. Briggs, R. Gold, and J. Thompson Jobe (2022). Geologic model of deformation for the 2023 update to the US National Seismic Hazard Model, *Seismol. Res. Lett.* in preparation.

Hearn, E. (2019). Kinematics of southern California crustal deformation: Insights from finite-element models, *Tectonophysics*, doi: 10.1016/j.tecto.2019.02.016.

Hearn, E. H. (2022). Evaluation of viscoelastic-cycle effects on instantaneous deformation rates for the 2023 update to the US National Seismic Hazard Model, *Seismol. Res. Lett.* (in press).

Hearn, E. H., F. F. Pollitz, W. R. Thatcher, and C. T. Onishi (2013). How do ghost transients from past earthquakes affect GPS slip rate estimates on southern California faults? *Geochem. Geophys. Geosys.* **14,** 828–838.

Johnson, K. M. (2013). Slip rates and off-fault deformation in southern California inferred from GPS data and models, *J. Geophys. Res.* **118,** no. 10, 5643–5664.

Johnson, K. M., C. Wespestad, and J. Murray (2022). Creep rate data and models for the 2023 update to the US National Seismic Hazard Model, *Seismol. Res. Lett.* (in press).

Kagan, Y. Y. (2009).Testing long-term earthquake forecasts: Likelihood methods and error diagrams, *Geophys. J. Int.* **177,** no. 2, 532–542.

Liu, Z., and P. Bird (2008). Kinematic modelling of neotectonics in the Persia-Tibet-Burma Orgen, *Geophys. J. Int.* **172,** no. 2, 779–797.

McCaffrey, R., R. W. King, S. J. Payne, and M. Lancaster (2013). Active tectonics of northwestern US inferred from GPS-derived surface velocities, *J. Geophys. Res.* **118,** no. 2, 709–723.

Nazareth, J. J., and E. Hauksson (2004). The seismogenic thickness of the southern California crust, *Bull. Seismol. Soc. Am.* **94,** no. 3, 940–960.

Parsons, T., K. M. Johnson, P. Bird, J. Bormann, T. E. Dawson, E. H. Field, W. C. Hammond, T. A. Herring, R. McCaffrey, Z.-K. Shen, *et al.* (2013). Appendix C: Deformation Models for UCERF3, E. H. Field *et al.* (Editor), Uniform California Earthquake Rupture Forecast, Version 3 (UCERF3)—The time-independent model, *U.S. Geol. Surv. Open-File Rept. 2013-1165 Cal. Geol. Surv. Spec. Rep. 228, and Southern California Earthquake Center Pub. 1792*, 97 pp.

Pollitz, F. F., and E. Evans (2017). Implications of the earthquake cycle for inferring fault locking on the Cascadia megathrust, *Geophys. J. Int.* **209,** 167–185, doi: 10.1093/gji/ggx009.

Powers, P. M., and E. H. Field (2015). 2014 Update to the National Seismic Hazard Model in California, *Earthq. Spectra* **31,** no. 1_suppl, S177–S200.

Schorlemmer, D., M. C. Gerstenberger, W. Wiemer, D. D. Jackson, and D. A. Rhoades (2007). Earthquake likelihood model testing, *Seismol. Res. Lett.* **78,** no. 1, 17–29.

Shen, Z.-K., R. King, D. Agnew, M. Wang, T. A. Herring, D. Dong, and P. Fang (2011). A unified analysis of crustal motion in southern California, 1970-2004: The SCEC crustal motion map, *J. Geophys. Res.* **116,** no. B11, doi: 10.1029/2011JB008549.

Wessel, P., and W. H. F. Smith (1998). New, improved version of Generic Mapping Tools released, *EOS Trans. AGU* **79,** no. 47, 579, doi: 10.1029/98EO00426.

Zechar, J. D., and T. H. Jordan (2008). Testing alarm-based earthquake predictions, *Geophys. J. Int.* **172,** 715–724, doi: 10.1111/j.1365-246X.2007.03676.x.

Zeng, Y. (2022). GPS velocity field of the western U.S. for the 2023 National Seismic Hazard Model Update, *Seismol. Res. Lett.* doi: 10.1785/0220220180.

Zeng, Y., and Z.-K. Shen (2016). A fault-based model for crustal deformation, fault slip rates and off-fault strain rate in California, *Bull. Seismol. Soc. Am.* **106,** no. 2, 766–784, doi: 10.1785/0120140250.

Manuscript received 2 June 2022
Published online 14 September 2022